



Title	Mesoscale simulation of bond behaviors between concrete and reinforcement under the effect of frost damage with axisymmetric Rigid Body Spring Model
Author(s)	Wang, Zhao; Zhang, Dawei; Gong, Fuyuan; Mehrpay, Saeid; Ueda, Tamon
Citation	Construction and building materials, 215, 886-897 https://doi.org/10.1016/j.conbuildmat.2019.04.232
Issue Date	2019-08-10
Doc URL	http://hdl.handle.net/2115/82436
Rights	© 2019. This manuscript version is made available under the CC-BY-NC-ND 4.0 license http://creativecommons.org/licenses/by-nc-nd/4.0/
Rights(URL)	http://creativecommons.org/licenses/by-nc-nd/4.0/
Type	article (author version)
File Information	[Zhao0811]Final Manuscript.pdf



[Instructions for use](#)

Mesoscale Simulation of Bond Behaviors between Concrete and Reinforcement under the Effect of Frost Damage with Axisymmetric Rigid Body Spring Model

Zhao Wang¹, Dawei Zhang², Fuyuan Gong^{3*}, Saeid Mehrpay⁴ and Tamon Ueda⁵

¹Laboratory of Engineering for Maintenance System, Graduate School of Engineering, Hokkaido University, Japan.

^{2,3}College of Civil Engineering and Architecture, Zhejiang University, China.

⁴Laboratory of Engineering for Maintenance System, Graduate School of Engineering, Hokkaido University, Japan.

⁵Laboratory of Engineering for Maintenance System, Faculty of Engineering, Hokkaido University, Japan.

Abstract

Frost damage is a key deterioration factor for concrete structures in cold and wet areas which has been studied for several decades. For reinforced concrete (RC) structures, bond between reinforcement and concrete plays an important role and its degradation under freezing-thawing environment would affect the service life of the RC structures. This paper aims to develop a mesoscale simulation approach which could estimate and investigate the bond behaviors under the effect of frost damage. Based on the axisymmetric discrete element model - Rigid Body Spring Model, the micro-mesoscale mechanical strengthening/damaging effects by frost action were implemented to non-air entrained concrete and the bond interface. One-way pulling-out test was simulated and the calculated bond strength was compared with experimental results where good agreement was found.

Keywords: bond behavior; frost damage; axisymmetric Rigid Body Spring Method; mesoscale simulation.

1. Introduction

Frost damage is one of the important environmental actions for life-cycle evaluation of reinforced concrete structures. Lots of studies have revealed that the damage induced by freezing and thawing cycles would affect the reinforced concrete structures in two aspects: degradation of mechanical properties of concrete and bond behaviors between concrete and reinforcement [1, 2]. Thus, to understand and quantify the effect of frost damage on the material and bond properties has become urgent and important so that the assessing of RC structural behaviors under frost damage such as load carrying capacity could be achieved using finite element analysis.

A lot of researches have been conducted to disclose the mechanisms of frost damage on concrete materials. It is generally agreed that several types of forces occur during the ice formation and the damage by frost action could be quite different with different material and environmental conditions [3-5]. For open ambient condition where continuous water was supplied, non-AE concrete showed unrecoverable plastic deformation with increasing number of freezing-thawing cycles (FTCs) [6-7]. Under this circumstance, both simulation and experiments found that accompanied with the accumulation of frost damage, the compressive strength, tensile strength and elastic modulus decreased while the compressive strain at peak stress increased [6, 8-12]. On basis of the simulation

1 results or experimental data, mechanical degradation models of concrete (including compressive
2 and tensile behaviors) were proposed, which could be adopted in finite element analysis [10-14].

3 Although many research articles have primarily concerned about the deteriorated properties of
4 frost-damaged concrete, very limited attention has been given to the effect of freezing-thawing
5 cycles on the bond behaviors between concrete and reinforcement. Pulling-out experimentations
6 with specimens of short embedment length could be found which investigated the local bond-slip
7 relationship between concrete and reinforcement under the effect of frost damage [1, 15-18]. Shih
8 conducted concentric pulling-out test with prismatic specimens to find that the cyclic temperature
9 change affected both bond strength and bond-slip curve [15]. Peterson et al. carried eccentric
10 pulling-out test on cubic specimens with only one-surface suffering frost damage according to the
11 TC 176 IDC test standard [11, 19]. The results showed that with increasing number of FTC, the
12 bond strength decreased but the slip at peak bond stress showed slightly decreasing for the first few
13 cycles and then increased. By contrast, other experiments indicated continuous increase of slip at
14 peak bond stress and reduction of bond strength accompanied with more FTCs [1, 2, 17, 18]. Liu et
15 al. proved that the bond between reinforcement and TIC (thermal insulation concrete) could have a
16 better resistance against frost damage than the bond between reinforcement and normal concrete
17 due to the special porous structures of TIC [18]. Due to the complexity of bond mechanism and frost
18 damage mechanism, the simulation work of bond behaviors under cyclic freezing-thawing
19 environment is still lacking as far as the authors' knowledge.

20 In this study, a mesoscale simulation program was developed to investigate the bond
21 degradation under frost damage based on the axisymmetric discrete element model - Rigid Body
22 Spring Method (RBSM). Only non-air entrained case was focused since the effectiveness of air-
23 entraining-agent depends largely on its type and quality which makes its working mechanism
24 complicated and still unclear. Besides, the simulation program and models of bond behaviors for
25 non-air entrained case are lacked at this moment which is needed urgently for future studies. A
26 unified mechanical model considering the contribution of ice-strengthened elastic properties, pre-
27 stored pore pressure during freezing as well as the meso-cracks was implemented into the
28 axisymmetric RBSM program. One-way pulling-out test was simulated after a whole process of
29 FTC. The simulated bond-slip relationships for both sound (non-damaged) and damaged specimens
30 were also compared with previous experiments where good agreements were found to support the
31 reliability and applicability of the program. Parametric study is hopefully to be conducted with this
32 program in the future to propose a simulation-based deterioration model of bond-slip relationship,
33 which can be adopted in the numerical structural analysis of reinforced concrete members.

34 35 **2. Axisymmetric Rigid Body Spring Method**

36 **2.1 Review of RBSM**

37 The Rigid Body Spring Method is a discrete numerical analysis method firstly developed by
38 Kawai in 1978 [20]. Different from the continuum applications such as Finite Element Method or
39 Finite Difference Method, RBSM is a more proper way pertaining to simulate the cracking issues
40 for cementitious materials like concrete and mortar [8, 9, 21, 22]. Besides, RBSM is more suitable
41 for small deformation and tiny cracks which are often seen in concrete structures compared with
42 other discrete method such as Distinct Element Method. Since it is generally accepted that bond
43 action between concrete and deformed reinforcement bars are mainly assured by the interlocking
44 between ribs of rebar and intercostal concrete, and bond failure always accompanies with transverse

cracking and splitting cracking of concrete, Rigid Body Spring Method is preponderant to simulate the bond behaviors than other numerical methods [2, 23].

Several researches have been conducted on developing the Rigid Body Spring Method for concrete materials and reinforced concrete structures: Kawai brought up the concept of 2D plane stress/strain RBSM and gave some discussions on basis of the simulation examples using triangle elements [20]. Bolander and Saito introduced truss reinforcement elements as well as polyhedron concrete elements and they applied the RBSM approach to analyze concrete and reinforced concrete beams [24]. Muto et al. adopted 2D reinforcement elements by configuring the outline of ribs and simulated uniaxial pulling-out test with specimens of long embedment length [25]. Tension stiffening was successfully observed in their simulation and the effect of several parameters were discussed. Nagai et al. developed mesoscale 2D plane stress RBSM program and 3D RBSM program for concrete by separating the model into mortar, aggregate and the interfacial transition zone (ITZ) between them [21, 26]. The mesoscopic 2D plane stress RBSM program was adopted to simulate the uniaxial/biaxial mechanical test and the bending test for concrete and mortar [20, 22, 27]. Through integrating the internal pressure model due to ice formation as well as the constitutive models of springs accounting for frost action and fatigue, Gong et al. developed the mesoscale 2D plane stress RBSM application to simulate the monotonic and fatigue behaviors of frost-damaged concrete which was supported by the experiment results [5, 6, 7, 22, 27]. Recently, Hayashi et al. conducted modeling of reinforcement elements with geometric shape with 3D RBSM in which the RC anchorage performance was analyzed and verified [28].

To achieve further understanding on the bond deterioration owing to frost damage, the corresponding mesoscale RBSM approach needs to be developed which unfortunately is still in lack. However, bond action between concrete and deformed bars is a three-dimensional issue where hoop stresses in concrete exist to resist the outward component of the interactive pressure between rebar and concrete. Thus, the 2D plane stress/strain RBSM program could no longer be applied [8, 9, 21, 27]. 3D RBSM program could perform the bond behaviors properly but consume plenty of time due to the large number of elements in mesoscale case, especially for the calculation time of frost damage process [22, 26, 28]. Therefore, the mesoscale axisymmetric Rigid Body Spring Method was developed to avoid the extremely large consumption of calculation time.

2.2 Mesoscale axisymmetric RBSM

Axisymmetric modeling technique is a two-dimensional analytical method which unlike 2D plane stress/strain methods can evaluate the out-of-plane stress and strain components as well. In the polar system, circumferential strain and stress of the element will initiate once deformation takes place in the radial direction [29-31].

The mesoscale axisymmetric RBSM model is divided into polyhedron elements with random mesh using Voronoi diagram and the elements are assumed to be connected by springs. Each Voronoi cell represents a mortar, aggregate or reinforcement element with two translational and one rotational degree of freedom locating at the center of gravity of the element. For two adjacent elements, there are three springs connecting, i.e. normal spring, shear spring and circumferential spring, which are placed at the midpoint of boundary between two elements (see **Fig. 1**). As suggested by Takeuchi et al., the stiffness values of springs K_{sp} are evaluated from Eq. (1) where subscripts n , φ and s stand for normal spring, circumferential spring and shear spring, respectively [29]. E_{elem} and ν_{elem} are accordingly the mesoscopic elastic modulus and Poisson's ratio of the

element (mortar, aggregate or reinforcement), which can be derived from the macroscale material properties as Eq. (2) [26].

$$\begin{cases} Ksp_n = Ksp_\varphi = \frac{(1 - \nu_{elem})E_{elem}}{(1 + \nu_{elem})(1 - 2\nu_{elem})} \\ Ksp_s = \frac{E_{elem}}{2(1 + \nu_{elem})} \end{cases} \quad (1)$$

$$\begin{aligned} \nu_{elem} &= -24.8v^4 + 31.9v^3 - 16.4v^2 + 4.28v \\ E_{elem} &= E(-33.7v_{elem}^4 + 17.0v_{elem}^3 - 4.13v_{elem}^2 + 0.327v_{elem} + 1) \end{aligned} \quad (2)$$

For normal and shear springs of mortar-aggregate interface, the stiffness K is given as weighted average of mortar and aggregate, as shown in Eq. (3) [21]. In which, h is the length of the perpendicular line from the centroid of element to the boundary, see **Fig. 1**. For normal and shear springs of mortar-reinforcement (bond) interface, the values of stiffness are assumed same as those for mortar according to Muto et al. [25]. It should be noted that for circumferential springs, the values of stiffness for mortar-reinforcement (bond), mortar-mortar, mortar-aggregate (ITZ) and aggregate-aggregate interfaces are calculated using E_{elem} and ν_{elem} of mortar.

$$\begin{cases} K_n = \frac{Ksp_{n1}h_1 + Ksp_{n2}h_2}{h_1 + h_2} \\ K_s = \frac{Ksp_{s1}h_1 + Ksp_{s2}h_2}{h_1 + h_2} \end{cases} \quad (3)$$

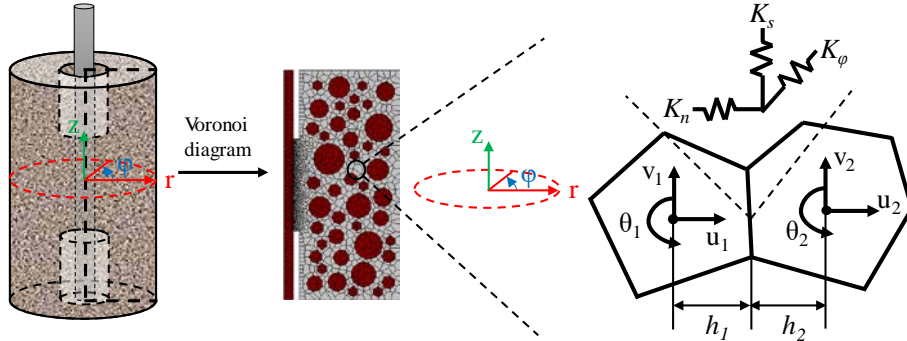


Fig. 1. Schematic of mesoscale axisymmetric RBSM model

A normal distribution is simply assumed for the tensile strength of normal springs since concrete/mortar is not a homogeneous material, see Eq. (4). In Eq. (4), $f_{t,elem}$ is the tensile strength of the element and assuming $f_{t,elem}=0$ when $f_{t,elem}<0$; μ is the average value of $f_{t,elem}$ and s is the standard derivation [21].

$$f(f_{t,elem}) = \frac{\exp\left[-(f_{t,elem} - \mu)^2 / 2s^2\right]}{\sqrt{2\pi}s} \quad (4)$$

$$s = -0.2\mu + 1.5$$

For the shear springs of mortar, an elasto-plastic criterion is adopted where the value of maximum shear strength τ_{max} changes based on the status of normal springs, see Eq. (5) [26]:

$$\tau_{\max} = \pm \left(0.30 f_{t,elem}^{2.5} (-\sigma + f_{t,elem})^{0.4} + 0.15 f_{t,elem} \right) \quad (5)$$

in which σ is the normal stress. And for the shear springs of mortar-reinforcement (bond) and mortar-aggregate (ITZ) interfaces, the shear criterion follows Eq. (6):

$$\tau_{\max} = \pm (\sigma \tan \theta + c_i) \quad (6)$$

where θ and c_i are constant values. For shear springs of mortar, ITZ and bond interface, the ideal plastic performance is assumed when local shear strain is small [25, 26]. Whereas the shear stress transfer will decrease when shear sliding becomes big and the attached length of two elements is significantly reduced. In addition, the shear strength and stiffness could also be affected by the normal tensile cracking. Thus, the following reduction rule is considered for the shear behaviors [22].

$$\begin{aligned} \tau_{\max}' &= \tau_{\max} (1 - \delta_s / l_{elem}) (1 - w / w_{\max}) \\ K_s' &= K_s (1 - \delta_s / l_{elem}) (1 - w / w_{\max}) \end{aligned} \quad (7)$$

where δ_s and l_{elem} are the sliding distance and length of attaching boundary between the adjacent elements; w is the crack width in normal direction and w_{\max} is the maximum crack width for different components. Similarly, considering that the tensile stress transfer might be reduced by the shear sliding at same location, linear reduction is adopted for the tensile behavior as Eq. (8). The above effects have been verified by the previous simulation of uniaxial compression and biaxial compression-tension tests [21, 22]. Besides, for circumferential springs of mortar-reinforcement (bond), mortar-mortar, mortar-aggregate (ITZ) and aggregate-aggregate interfaces, the values of tensile strength are set the same as ITZ for consideration that ITZ usually acts as the weakest part and dominates the circumferential behaviors.

$$\begin{aligned} f_{t,elem}' &= f_{t,elem} (1 - \delta_s / l_{elem}) \\ K_n' &= K_n (1 - \delta_s / l_{elem}) \end{aligned} \quad (8)$$

2.3 Stiffness matrix for axisymmetric RBSM

To develop the mesoscale axisymmetric RBSM, the stiffness matrix is essential and the derivation is stated as the following process: naming $\mathbf{u} = [u_{P1} \ v_{P1} \ u_{P2} \ v_{P2}]^T$ and $\mathbf{u}_e = [u_1 \ v_1 \ \theta_1 \ u_2 \ v_2 \ \theta_2]^T$ to be the displacement vectors of mid-point of interface between two adjacent elements (point P) and elemental centroids (point 1 and 2) in global z-r- ϕ polar coordinate system, see Fig. 2.

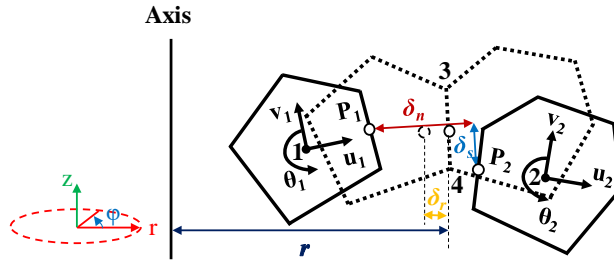


Fig. 2 Illustration of two adjacent elements in axisymmetric RBSM

Then the relationship between \mathbf{u} and \mathbf{u}_e is given as Eq. (9), where $x_{ij} = x_i - x_j$ and $y_{ij} = y_i - y_j$:

$$\mathbf{u} = \mathbf{Q} \mathbf{u}_e$$

$$\mathbf{Q} = \begin{bmatrix} 1 & 0 & y_P - y_1 & \mathbf{0} \\ 0 & 1 & -(x_P - x_1) & \\ & & 1 & 0 & y_P - y_2 \\ & & 0 & 1 & -(x_P - x_2) \end{bmatrix} = \begin{bmatrix} 1 & 0 & y_{P1} & \mathbf{0} \\ 0 & 1 & -x_{P1} & \\ & & \mathbf{0} & 1 & 0 & y_{P2} \\ & & & 0 & 1 & -x_{P2} \end{bmatrix} \quad (9)$$

Converting the displacement of point P from global polar coordinate system (z-r-φ) into local orthogonal coordinate system (n-s) where normal and shear springs locate, it yields that:

$$\mathbf{u} = \mathbf{R} \mathbf{u}$$

$$\mathbf{R} = \begin{bmatrix} \cos \theta_n & \sin \theta_n & \mathbf{0} \\ -\sin \theta_n & \cos \theta_n & \\ & \mathbf{0} & \cos \theta_n & \sin \theta_n \\ & & -\sin \theta_n & \cos \theta_n \end{bmatrix} = \frac{1}{l_{43}} \begin{bmatrix} -y_{43} & x_{43} & \mathbf{0} \\ -x_{43} & -y_{43} & \\ & \mathbf{0} & -y_{43} & x_{43} \\ & & -x_{43} & -y_{43} \end{bmatrix} \quad (10)$$

where $\mathbf{u} = [\underline{u}_{P1} \ \underline{v}_{P1} \ \underline{u}_{P2} \ \underline{v}_{P2}]^T$ is the displacement vector of point P in local coordinate system. θ_n stands for the angle between interface and r-direction. l_{43} represents the length between point 3 and 4, as shown in Fig. 2. Once the displacements of point P are given, the spring deformation vector $\mathbf{d} = [\delta_n \ \delta_r \ \delta_s]^T$ of point P could be calculated, referring to Eq. (11). δ_n and δ_s represent the deformation of normal and shear springs. δ_r stands for the deformation in r-direction, which in other words, is the translational movement of point P towards the z-axis, see Fig. 2.

$$\mathbf{d} = \mathbf{M} \mathbf{u}$$

$$\begin{Bmatrix} \delta_n \\ 2\delta_r \\ \delta_s \end{Bmatrix} = \begin{bmatrix} -1 & 0 & 1 & 0 \\ \cos \theta_n & -\sin \theta_n & \cos \theta_n & -\sin \theta_n \\ 0 & -1 & 0 & 1 \end{bmatrix} \begin{Bmatrix} \underline{u}_{P1} \\ \underline{v}_{P1} \\ \underline{u}_{P2} \\ \underline{v}_{P2} \end{Bmatrix} = \begin{bmatrix} -1 & 0 & 1 & 0 \\ -y_{43}/l_{43} & -x_{43}/l_{43} & -y_{43}/l_{43} & -x_{43}/l_{43} \\ 0 & -1 & 0 & 1 \end{bmatrix} \begin{Bmatrix} \underline{u}_{P1} \\ \underline{v}_{P1} \\ \underline{u}_{P2} \\ \underline{v}_{P2} \end{Bmatrix} \quad (11)$$

Combing Eq. (9), (10) and (11), it indicates that the relationship between $\mathbf{u}_e = [u_1 \ v_1 \ \theta_1 \ u_2 \ v_2 \ \theta_2]^T$ and $\mathbf{d} = [\delta_n \ \delta_r \ \delta_s]^T$ follows:

$$\mathbf{d} = \mathbf{N} \mathbf{u}_e$$

$$\mathbf{N} = \mathbf{M} \mathbf{R} \mathbf{Q} = \frac{1}{l_{43}} \begin{bmatrix} y_{43} & -x_{43} & x_{43}x_{P1} + y_{43}y_{P1} & -y_{43} & x_{43} & -x_{43}x_{P2} - y_{43}y_{P2} \\ \frac{l_{43}}{2} & 0 & \frac{l_{43}y_{P1}}{2} & \frac{l_{43}}{2} & 0 & \frac{l_{43}y_{P2}}{2} \\ x_{43} & y_{43} & x_{43}y_{P1} - y_{43}x_{P1} & -x_{43} & -y_{43} & -x_{43}y_{P2} + y_{43}x_{P2} \end{bmatrix} \quad (12)$$

The relationship between spring deformation vector $\mathbf{d} = [\delta_n \ \delta_r \ \delta_s]^T$ and spring strain vector $\boldsymbol{\varepsilon} = [\varepsilon_n \ \varepsilon_\varphi \ \varepsilon_s]^T$ follows Eq. (13):

$$\boldsymbol{\varepsilon} = \begin{Bmatrix} \varepsilon_n \\ \varepsilon_\varphi \\ \varepsilon_s \end{Bmatrix} = \begin{Bmatrix} \delta_n / (h_1 + h_2) \\ \delta_r / r \\ \delta_s / (h_1 + h_2) \end{Bmatrix} = \mathbf{B} \mathbf{u}_e$$

$$\mathbf{B} = \frac{1}{l_{43}} \begin{bmatrix} y_{43}/h & -x_{43}/h & (x_{43}x_{P1} + y_{43}y_{P1})/h & -y_{43}/h & x_{43}/h & (-x_{43}x_{P2} - y_{43}y_{P2})/h \\ \frac{l_{43}}{2r} & 0 & \frac{l_{43}y_{P1}}{2r} & \frac{l_{43}}{2r} & 0 & \frac{l_{43}y_{P2}}{2r} \\ x_{43}/h & y_{43}/h & (x_{43}y_{P1} - y_{43}x_{P1})/h & -x_{43}/h & -y_{43}/h & (-x_{43}y_{P2} + y_{43}x_{P2})/h \end{bmatrix} \quad (13)$$

where h_i is the length of the perpendicular line from the centroid of element to the boundary ($h = h_1 + h_2$), see Fig. 1. r is the radial distance between point P and the axis, see Fig. 2. According to

the theories of mechanics of elastic bodies, the stress-strain relationship for springs in axisymmetric model is:

$$\begin{Bmatrix} \sigma_n \\ \sigma_\varphi \\ \sigma_s \end{Bmatrix} = \mathbf{D} \begin{Bmatrix} \varepsilon_n \\ \varepsilon_\varphi \\ \varepsilon_s \end{Bmatrix} = \begin{bmatrix} \frac{(1-\nu)E}{(1+\nu)(1-2\nu)} & 0 & 0 \\ 0 & \frac{(1-\nu)E}{(1+\nu)(1-2\nu)} & 0 \\ 0 & 0 & \frac{E}{2(1+\nu)} \end{bmatrix} \begin{Bmatrix} \varepsilon_n \\ \varepsilon_\varphi \\ \varepsilon_s \end{Bmatrix} \quad (14)$$

In Eq. (14), σ and ε means stress and strain, and subscripts n , s and φ represent normal, shear and circumferential direction, respectively. Applying the principle of virtual work, if small displacement \mathbf{u}_e^* is assumed to take place on the adjacent elements, the corresponding strain of springs would be $\boldsymbol{\varepsilon}^*$:

$$\{\mathbf{u}_e^*\}^T \mathbf{f}_e = \int \{\boldsymbol{\varepsilon}^*\}^T \mathbf{\sigma} \quad (15)$$

where \mathbf{f}_e is the force vector of element centroids (point **1** and **2**). Considering the spring lengths and effective areas, the right term of Eq. (15) could be transformed according to Eq. (13) and (14):

$$\int \{\boldsymbol{\varepsilon}^*\}^T \mathbf{\sigma} = \{\mathbf{B} \mathbf{u}_e^*\}^T \begin{bmatrix} h_1+h_2 & 0 & 0 \\ 0 & 2\pi r & 0 \\ 0 & 0 & h_1+h_2 \end{bmatrix} \begin{bmatrix} l_{43} \times 2\pi r & 0 & 0 \\ 0 & l_{43} \times (h_1+h_2) & 0 \\ 0 & 0 & l_{43} \times 2\pi r \end{bmatrix} \mathbf{D} \mathbf{B} \mathbf{u}_e \quad (16)$$

Substitute Eq. (16) into Eq. (15) and eliminate the term of $\{\mathbf{u}_e^*\}^T$, it yields that:

$$\begin{aligned} \mathbf{f}_e &= 2\pi r l_{34} (h_1+h_2) \mathbf{B}^T \mathbf{D} \mathbf{B} \mathbf{u}_e = \mathbf{K} \mathbf{u}_e \\ \mathbf{K} &= 2\pi r l_{34} (h_1+h_2) \mathbf{B}^T \mathbf{D} \mathbf{B} \end{aligned} \quad (17)$$

Finally, the stiffness matrix \mathbf{K} is derived for mesoscale axisymmetric Rigid Body Spring Method.

3. Micro-mesoscale Models for FTC

In the mesoscale axisymmetric RBSM program, mechanical models are required in mesoscale which account for the concrete behaviors under the effect of FTCs. The main influences from the ice formation are explained in the following statements by separating the influencing scale into microscale and mesoscale. At microscale level, the representative volume elements (mortar Voronoi cells in **Fig. 1**) are adopted which compose of cement matrix and pore space (filled with ice, liquid and air). In this stage, the internal pore pressure is transferred into an equivalent volumetric force while the pore ice leads to higher elastic mechanical properties such as elastic modulus, Poisson's ratio and strength. At mesoscale level, springs connecting the representative volume elements are adopted where the internal pore pressure is treated as pre-stressed condition and the ice-enhanced properties are directly considered in the constitutive laws. In this stage, meso-cracks form in normal and circumferential springs if the ice volume expansion is big. With the above micro-mesoscale models, the macroscale compression of pure concrete as well as the pulling-out behaviors of reinforcement from concrete under the effect of frost damage could be simulated with axisymmetric RBSM.

3.1 Ice content evaluation

As a key factor to evaluate the internal pressure during freezing-thawing cycles, the amount of ice content needs to be evaluated. To calculate the ice content, it is essential to know the freezing point of pore water as well as the pore size distribution. The freezing point of pores with certain radius (r_0) could be calculated based on Eq. (18) where $\gamma_{CL} \approx 0.04 \text{ J/m}^2$ is the specific energy of crystal/liquid surface; $\Delta S_{fv} \approx 1.2 \text{ J/cm}^3 \text{ K}$ is the molar entropy of fusion; T_0 is for certain freezing temperature in Kelvin unit; $\delta \approx 0.9 \text{ nm}$ is the thickness of liquid film between the ice crystal and the pore wall [5, 32]:

$$r_0 = -\frac{2\gamma_{CL}}{T_0 \Delta S_{fv}} + \delta \quad (18)$$

The authors have proposed an empirical pore size distribution based on the water adsorption test by Xi et al., which considers a wide range of parameters such as water/cement ratio, curing age and temperature etc., as shown in Eq. (19) [33].

$$V(r \geq r_0) = \frac{(W_{sat} - W(r_0)) / \rho_{wat}}{1 / \rho_{solid} + W_{sat} / \rho_{wat}} \quad (19)$$

$$= \frac{1 / \rho_{wat}}{1 / \rho_{solid} + W_{sat} / \rho_{wat}} \left\{ W_{sat} - \frac{CkV_m(RH)}{[1 - k(RH)][1 + (C - 1)k(RH)]} \right\}$$

where $V(r \geq r_0)$ means the absolute volume of pores with larger radius than r_0 in unit volume of cement paste; W_{sat} stands for the normalized water content by weight of cement paste; ρ is the density of substance; RH is the relative humidity; The values of W_{sat} and RH could be calculated as Eq. (20) in which $\gamma_{LV} \approx 0.072 \text{ J/m}^2$ is the specific energy of liquid/vapor surface; $v_l = 1.8 \times 10^{-5} \text{ m}^3/\text{mol}$ is the molar volume of water; $R = 8.314 \text{ J/K/mol}$ is the ideal gas constant; T is the absolute temperature; $\delta' = 10^{-9} (0.834RH + 0.0626 + 0.02309(1.105 - RH)^{-1})$ is the thickness of adsorbed liquid-like layer [32]. The other parameters could be calculated based on Gong et al., see Eq. (21) [32].

$$W_{sat} = \frac{CkV_m}{(1 - k)(1 + (C - 1)k)} \quad (20)$$

$$RH = \exp\left(-\frac{2\gamma_{LV}}{r_0 - \delta'} \frac{v_l}{RT}\right)$$

$$\begin{cases} V_m = 0.9 \left(0.068 - \frac{0.22}{t} \right) \left(0.85 + 0.45 \frac{w}{c} \right) \\ k = \frac{(1 - 1/n)C - 1}{C - 1} \\ n = 1.1 \left(2.5 + \frac{15}{t} \right) \left(0.33 + 2.2 \frac{w}{c} \right) \\ C = \exp\left(\frac{855}{T}\right) \end{cases} \quad (21)$$

In Eq. (21), t is the curing age and w/c is the water cement ratio. Then the ice content ψ_c at specific temperature T_0 could be calculated by combining Eq. (18) and (19), as shown in Eq. (22).

$$\psi_c(T_0) = \int_{r_0}^{\infty} V(r) dr = \int_{-2\gamma/(T_0 \Delta S_{fv}) + \delta}^{\infty} V(r) dr \quad (22)$$

3.2 Microscale model of internal pressure and strengthening

It has been widely believed that multi pressures exists during the ice formation including hydraulic pressure, cryosuction pressure and crystallization pressure [5, 22, 32]. Quantitation of hydraulic pressure depends on many factors such as saturation degree, entrained air content, permeability, plastic volume expansion of matrix, cooling rate etc. while cryosuction/ crystallization pressures are mainly depending on temperature and pore size distribution. For convenience, only summarized equations is given in Eq. (23) since detailed discussions could be found in the previous studies [5, 22, 32].

$$0.09\phi\dot{\psi}_c - \frac{A}{V} \frac{m}{\eta} \frac{2}{R_E - r_E} p_h = \left(\frac{b}{K_p} + \frac{\phi\psi_c}{K_c} + \frac{\phi\psi_l}{K_l} \right) \dot{p}_h$$

$$p_l = \psi_l \cdot \Delta S_{fv} \Delta T$$

$$p_c = -\psi_c \cdot (1 - \lambda) \Delta S_{fv} \Delta T$$
(23)

where p is the pressures with subscripts h , l and c standing for hydraulic, cryosuction and crystallization pressure, respectively; K_c and K_l are the bulk moduli of ice and liquid water with value of approximately 8.8 and 2.2 GPa; ψ_c and ψ_l represent the volume fraction of ice and liquid water in pore space; ϕ is the porosity; m is the permeability of the porous body; η is the viscosity of liquid water; b is the Biot coefficient; r_E and R_E are the equivalent radii of the entrained air and influential radius (average spacing factor between air voids $L=2R_E$); A and V are the equivalent empty space and influential volume; $\lambda=-0.0095T+0.125$ is the pore shape factor [34]; $\Delta S_{fv}=1.2\text{J}/\text{cm}^3$ and $\Delta T \leq 0$ are the molar entropy of fusion and temperature in Celsius, respectively. As a result, the effective stress σ_0 due to ice formation on porous body would be:

$$\sigma_0 = b(p_h + p_l + p_c)$$
(24)

Besides the internal pressure by ice formation, the effective elastic properties of representative volume elements are also estimated. Based on various literatures, the authors have developed a model for microscale representative volume elements composing with cement matrix, ice, liquid water and air, and upscale it to mesoscale mortar [32]. The homogenized bulk (K^{hom}) and shear (G^{hom}) moduli for a general n-phase composite are calculated as:

$$\begin{cases} K^{\text{hom}} = \sum_1^n f_r K_r P_r / \sum_1^n f_r P_r \\ G^{\text{hom}} = \sum_1^n f_r G_r Q_r / \sum_1^n f_r Q_r \end{cases}$$
(25)

in which f_r is the volume fraction of phase r ; P_r and Q_r stand for the compressibility and shear compliance of phase r . The expression of compressibility and shear compliance varies on different inclusion morphology of mortar level and cement paste level where detailed information could be found in Gong et al. [32]. With given K^{hom} and G^{hom} , the effective elastic modulus and Poisson's ratio are given according to Eq. (26).

$$E^{\text{hom}} = \frac{9K^{\text{hom}}G^{\text{hom}}}{3K^{\text{hom}} + G^{\text{hom}}}$$

$$\nu^{\text{hom}} = 0.5 \left(1 - \frac{1}{1/3 + K^{\text{hom}}/G^{\text{hom}}} \right)$$
(26)

3.3 Mesoscale constitutive laws

In mesoscopic level, for saturated concrete in non-freezing case, the normal and circumferential springs of mortar, ITZ and bond (see **Fig. 1**) behave linearly before the stress reaches the tensile strength f_t . Once the tensile strain exceeds the threshold value ε_0 , the stress will decrease linearly with increasing strain, see the black lines in **Fig. 3(a), (b)**. If freezing temperature is obtained and ice forms, enhanced elastic properties are taken into consideration for mortar, ITZ and bond. As a result, the elastic modulus of normal and circumferential springs of mortar, ITZ and bond interface would increase from k_n to k_n' . In other words, the constitutive curves of these springs would shift from the black lines to the red lines under freezing temperature in **Fig. 3(a), (b)**. Besides, it should be emphasized that no ice is assumed to take place in aggregate and rebar, thus the elastic modulus of normal springs of aggregate and rebar are not enhanced during the freezing temperature. As stated in Section 2.2, for the circumferential springs of aggregate-aggregate interfaces, the values of tensile strength are set the same as ITZ for consideration that ITZ usually acts as the weakest part and dominates the circumferential behaviors, the elastic modulus of circumferential springs of aggregate are enhanced since ice is considered to form in freezing temperature along the circumferential springs of aggregate-aggregate interfaces. However, the elastic modulus of circumferential springs of reinforcement are not enhanced due to no ice formation.

To consider the influence by frost damage, Ueda et al. developed a linear unloading-reloading path after the maximum historical strain reaches ε_0 , see the solid black curves in **Fig. 3(a), (b)** [27]. The envelope curve will point to a compressive strain ε_{pa} , which could be calculated based on experimental data [27, 32, 35]. It should be noted that two systems exist in the frozen cementitious material: the porous body system and ice-liquid system. The effective internal pressure due to ice formation $\sigma_0 = b(P_h + P_l + P_c)$ takes place firstly in the ice-liquid system. With expansion of the porous body, this effective pressure σ_0 is released until an equilibrium is achieved between two systems, referring to the intersection point in **Fig. 3(a)**. For convenience of the simulation, the internal pressure σ_0 is applied externally on both systems instead of internally on the ice-liquid system (**Fig. 3(b)**) as long as the final stress (σ_p) and strain (ε_{ta}) of porous body are same [8, 9, 22, 32]. Same effective internal pressure as mortar is applied on the bond interface and ITZ between mortar and aggregate for two reasons: 1. No obvious difference in the deformation of concrete after FTC and frost-damaged strength is found whether or not to apply a larger internal pressure on ITZ than mortar considering its larger porosity in the simulation of pure concrete. 2. For bond interface in pulling-out model, the potential larger expansion due to larger internal pressure than mortar can be restrained by surrounding concrete during FTC.

In the RBSM program, the deterioration of bond-slip behaviors includes two aspects: the degradation of concrete materials as well as the degradation of reinforcement-concrete interface. Besides, the ribs of reinforcement are also modeled because the concrete between ribs and near the tips of ribs will always show meso-cracks earlier than the other parts of concrete during the pulling-out. These meso-cracks in concrete near ribs will largely affect the bond-slip behaviors and such effect is aimed to be reflected in the simulation as well.

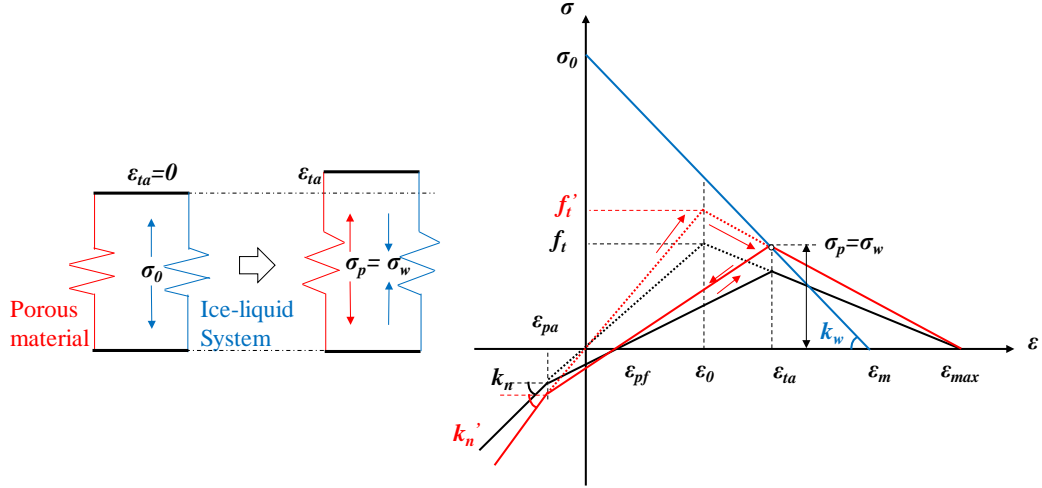


**Fig. 3(a). Constitutive relationship of normal and circumferential springs
(ice formation pressure added internally)**

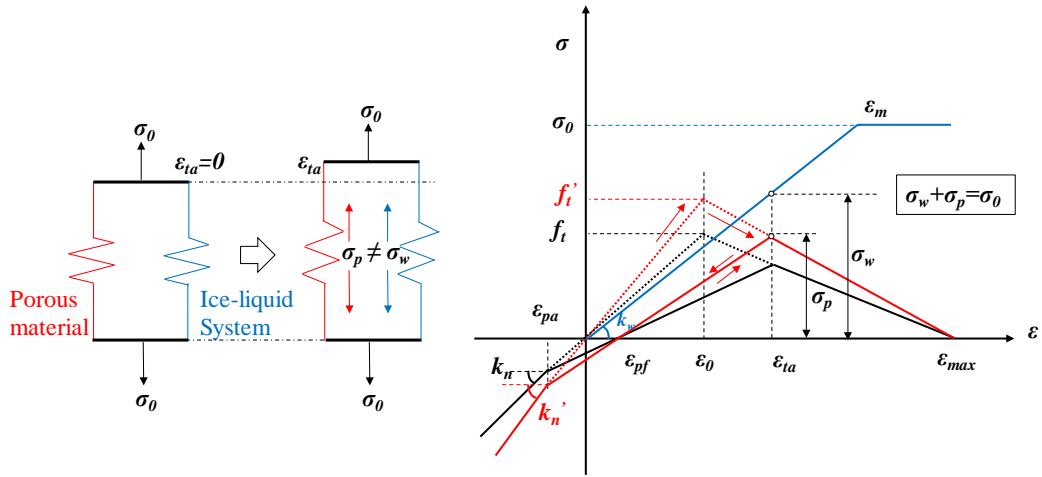


**Fig. 3(b). Constitutive relationship of normal and circumferential springs
(ice formation pressure added externally)**

Till now, all the essential models are available and programming work has been conducted using C++ language to build up the mesoscale axisymmetric RBSM which can simulate and analyze various mechanical behaviors such as compression and tension of pure concrete and bond-slip of pulling-out specimens after FTCs. Before simulating the bond properties with pulling-out models, the reliability and applicability of mesoscale axisymmetric RBSM program were investigated by simulating the uniaxial compression test of pure concrete specimens and uniaxial tension test of rebar.

4. Simulations and Discussions

4.1 Compression behaviors of plain concrete under FTC

To verify the mesoscale axisymmetric RBSM program, compression test of pure concrete under the effect of FTC was simulated using both mesoscale 2D plane stress RBSM and mesoscale

axisymmetric RBSM, and the simulation results were compared with existing experimental data.

Pure concrete specimens were modeled referring to the NC-C35 specimens in the experiment by Liu et al. in which air-entraining-agent was not adopted [18]. Objective compressive strength for non-damaged concrete was 39.28 MPa and the mix proportion was listed in **Table 1**. In previous studies, it was indicated that some macroscale material input values had relationships with the others, thus once one parameter was given the rest ones could be calculated, see Eq. (27) [21, 26]. In Eq. (27), f_{cm} is the compressive strength of mortar; E_m is the elastic modulus of mortar; f_{tp} is the pure tensile strength of mortar; f_{ti} is the tensile strength of ITZ of bond interface and mortar-aggregate interface; w/c is the water cement ratio and c_i is the parameter in interface criterion (Eq. (6)). It is indicated from Eq. (27) that the strength of ITZ is always less than that of mortar, which means the ITZ acts as the weakest part. Besides, as mentioned in section 2.2, the stiffness of bond interface is set same with that of mortar while the stiffness of ITZ between mortar and aggregate is assumed as the weight averaged value between two materials. Thus, mortar-aggregate interface has a higher stiffness than the bond interface. The number of coarse aggregates were distributed by size following the JSCE standard on basis of the volume fraction [21, 26, 36]. Cylindrical concrete specimens with dimension of $\Phi 100 \times 200$ mm was modeled by 2D plane stress RBSM and axisymmetric RBSM, see **Fig. 4**.

Table 1. Mix proportion of concrete (Liu et al. [18])

Type	Cement (kg/m ³)	Water (kg/m ³)	Sand (kg/m ³)	GHB* (kg/m ³)	Gravel (kg/m ³)	w/c
C30	239	127	490	156	970	0.53
C35	384	192	468	156	986	0.50
C40	417	200	440	156	1010	0.48

Note: *-In calculation of material inputs, GHB was neglect for NC-C35 specimens while GHB was assumed as coarse aggregate for TIC specimens, e.g. C30-5D, C40-5D, C35-3D and C35-6.5D in section 4.2.

$$\begin{aligned}
 E_m &= 1000 \left[7.7 \ln(f_{cm}') - 5.5 \right] \\
 f_{tp} &= 1.4(f_{cm}') - 1.5 \\
 c/w &= 0.047 f_{cm}' + 0.5 \\
 c_i &= -2.6w/c + 3.9 \\
 f_{ti} &= -1.44w/c + 2.3
 \end{aligned} \tag{27}$$

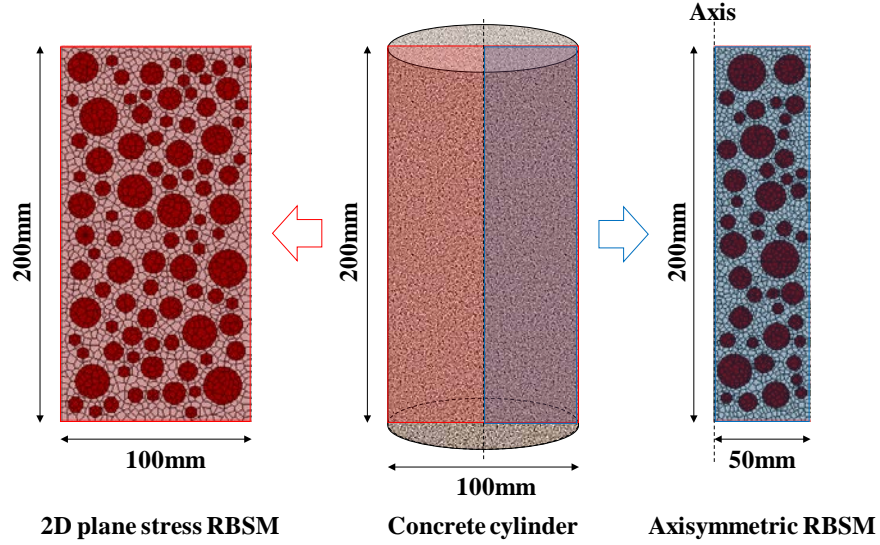


Fig. 4. Cylindrical concrete specimen, 2D plane stress RBSM and axisymmetric RBSM

The freezing and thawing cycles were firstly applied to the models before the compressive loading. It should be noted that simplification was made to neglect the effect of freezing and thawing rates so that much less computation time would be consumed. Previous studies had indicated such simplification did not affect the simulation results of final status of the frost-damaged specimens, which was the main interest of the study. According to Liu et al., the temperature varied from +20°C to -20°C in one cycle and three cases were prepared depending on the number of cycles (30, 60 and 100) [18]. After the FTC process, prescribed displacement loading with 0.005 mm/step was applied to the top surface of frost-damaged models. Meanwhile, restrictions of horizontal, vertical and rotational direction were given to the bottom surface of the specimens. The compressive stress-strain curves for non-damaged and frost-damaged concrete were drawn in **Fig. 5**, where “2D” and “Axi” represented the simulation results with 2D plane stress RBSM and axisymmetric RBSM, respectively; The numbers (0, 30, 60 and 100) afterwards stood for the numbers of freezing and thawing cycles. From **Fig. 5**, it yielded that good correlation was observed between two different models in which the compressive strength, strain at peak compressive stress as well as the stiffness in ascending branches showed satisfactory agreements. The cracking patterns of sound concrete by both models were drawn in **Fig. 6** where (a) and (d) showed the original models before compressive loading; (b) and (e) showed the post peak deformations where the deformations were enlarged by 10 times; (c) and (f) represented the cracking patterns in z-r plane where the red short lines meant the stress of normal spring had reached zero and become ineffective to sustain any load (strain of normal springs equaled to ε_{max} in **Fig. 3(a), (b)** and the crack width could be calculated according to the length of spring). Typical X-shape cracking was observed in 2D plane stress case as shown in **Fig. 6(c)**. Besides, the cracking shape could also be simulated with axisymmetric model, see **Fig. 6(f)**. It should be emphasized that the cracking of circumferential springs (in ϕ direction) was plotted in **Fig. 6(g)** where the blue spots meant that the strain of circumferential springs had reached ε_{max} . Compared with 2D plane stress RBSM, axisymmetric RBSM could give more information since it dealt with the issues of three-dimensional stress condition. In addition, the axisymmetric RBSM needed less computation time than the 2D plane stress RBSM even though it had finer mesh.

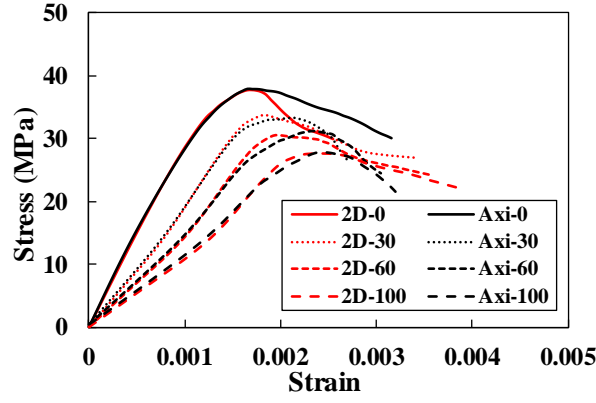


Fig. 5. Compressive stress-strain curves by 2D and axisymmetric RBSM

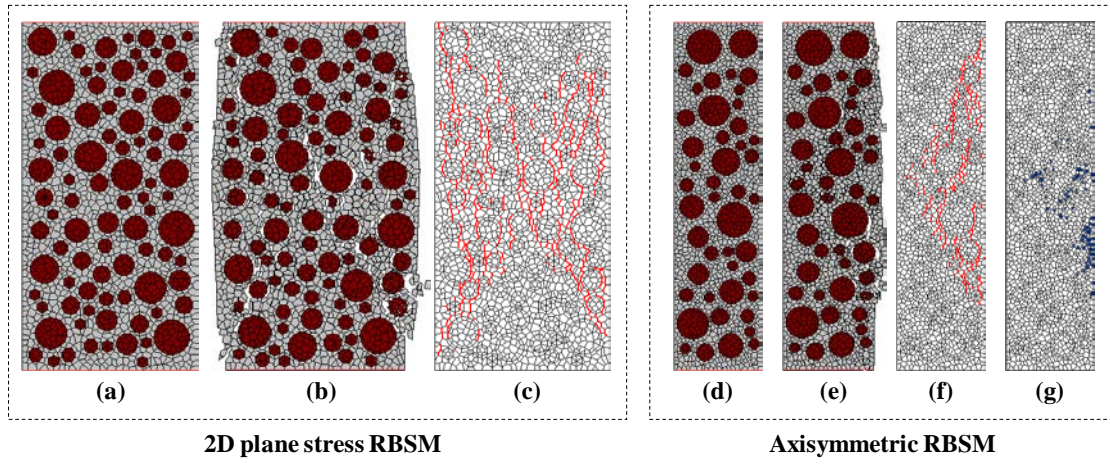


Fig. 6. Cracking patterns for sound concrete by 2D and axisymmetric RBSM

In addition, the experimental data of compressive strength degradation by Liu et al. [18] was also plotted together with the simulation results with both models, see Fig. 7. It had already been proved that the 2D plane stress RBSM could successfully predict the deteriorated compressive behaviors of concrete under FTC [9, 22, 32]. As shown in Fig. 7 where “2D” and “Axi” represented the simulation results with 2D plane stress RBSM and axisymmetric RBSM, the mesoscale axisymmetric RBSM developed in this study was proved to be reliable and adoptable to predict the material properties of frost-damaged concrete as well.

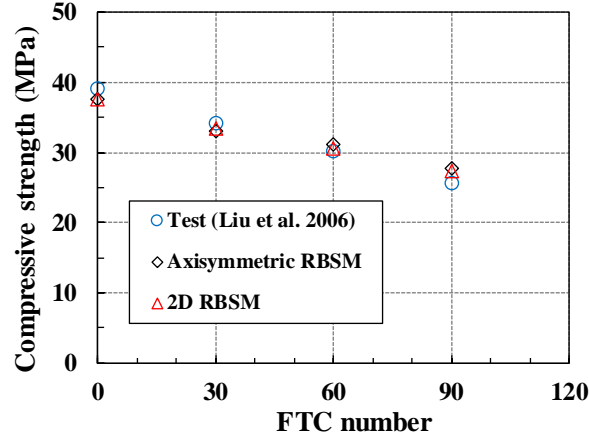


Fig. 7. Compressive strength degradation by test, 2D and axisymmetric RBSM

4.2 Pulling-out behaviors under FTC

Once the simulation by mesoscale axisymmetric RBSM on compressive behaviors of pure concrete under FTC had been verified, the pulling-out test was simulated and analyzed. Before simulating the pulling-out test, the elastic modulus and Poisson's ratio of reinforcement were evaluated, which was stated in Section 4.2.1. Afterwards, the pulling-out behaviors were simulated and analyzed for both sound specimens and frost-damaged specimens. The simulation model of pulling-out specimen was built up according to the specimens by Liu et al. [18]: for concrete, proportion was listed in **Table 1** and the non-frost damaged compressive strength was 39.28MPa; for reinforcement, hot-rolled ribbed bar (HRB) was used with diameter of 12mm and elastic modulus of 170GPa. Since the interactive action between ribs and concrete plays a rather important role in the bond behaviors when deformed reinforcements are adopted [2, 23], the precise configuration of ribs was considered in the model. Detailed information of reinforcement such as cross-sectional area (A_s), spacing between ribs (s_R), rib height (h_R) and rib width (w_R) could be found in the literature [18] and the values were listed in **Table 2**. The pulling-out model with embedment length of 5D was drawn in **Fig. 8**. In the experiment, plastic sleeves were adopted to insulate the un-bonded region of reinforcement from surrounding concrete so that the bond length could be ensured during casting and water could not penetrate directly from the ends of bond region during FTCs. The specimens were put into containers with 5 mm demineralized water of emerging where water could only penetrate from the surfaces (top, bottom and side surfaces) of concrete. As a result, an un-bonded area was also modeled in the RBSM program, as shown in **Fig. 8**.

Table 2. Morphology of HRB-D12 reinforcement (Liu et al. [18])

Type	A_s (mm ²)	s_R (mm)	h_R (mm)	w_R (mm)
HRB Φ 12	113.1	7.9	0.99	1.0

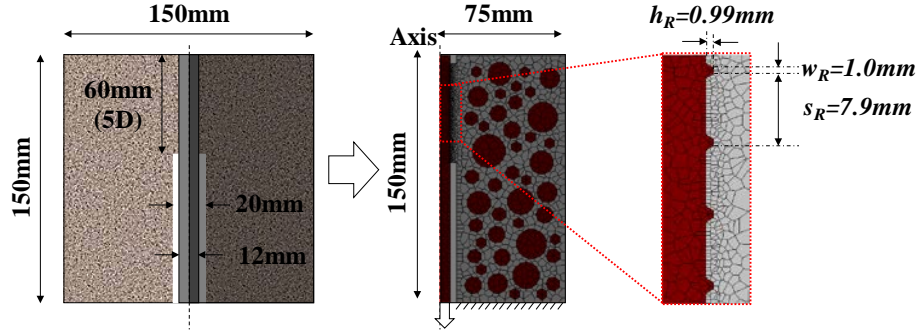


Fig. 8 Axisymmetric pulling-out model and details of ribs

It was noted that Liu et al. also prepared several thermal insulation pulling-out specimens with different embedment length (3D and 6.5D) and concrete strength (C30 and C40) by adding glazed hollow beads (GHB) [18]. Though the frost-damage resistance of such specimens was somehow difficult to be simulated in current study, simulating the pulling-out behaviors of those non-damaged specimens could offer supportive evidence for the reliability of the mesoscale axisymmetric RBSM program. Thus, for non-damaged pulling-out specimens, five cases were simulated depending on the embedment length (3D, 5D and 6.5D) and concrete strength (C30, C35 and C40), see **Table 3**. To model those specimens, the GHB was treated as aggregate as explained in **Table 1** as well. In **Table 3**, the models were named by “concrete strength grade-embedment length-FTC numbers”. For instance, “C35-5D-30” meant that the specimen was made of C35 (compressive strength=39.28 MPa) concrete and the embedment of reinforcement was 5D (60mm) which had suffered from 30 freezing and thawing cycles. Material inputs could be calculated according to Eq. (27) and FTC followed the same process as described in Section 3.1. Similar to the simulation of compression test of pure concrete, three damage cases were prepared where FTC stopped at the end of 30, 60 and 100 cycles together with one reference (non-damaged) case. Pulling-out simulation was conducted after the specimens had finished the corresponding numbers of FTCs. Prescribed displacement loading with 0.01 mm/step was applied to the bottom surface of reinforcement while the bottom surface of concrete was restrained in horizontal, vertical and rotational directions, see **Fig. 8**.

4.2.1 Uniaxial tension of rebar

Before conducting the pulling-out simulation, it was very important to investigate the uniaxial tensile behaviors of reinforcement by axisymmetric RBSM. For instance, owing to the Poisson’s ratio, radial contraction of rebar happened when the reinforcement was pulled out of the concrete and longitudinal elongation took place. This radial contraction would lead to delamination between the surface of reinforcement and the covering concrete, which affected the bond-slip behaviors. As a result, simulation of uniaxial tension was conducted with 200 mm D12 rebar where the ribs were neglected for simplification, see **Fig. 9** [18]. Since it was mentioned that no yielding of rebar was observed in the experiment, infinite yielding strength was given to the springs for reinforcement in the current program. In other words, only the elastic behaviors of rebar were verified and adopted in the simulation. The input elastic modulus and Poisson’s ratio of the reinforcement were 170GPa and 0.3, respectively. The simulated results were drawn in **Fig. 10** where the calculated elastic modulus and Poisson’s ratio were approximately 150GPa and 0.32, which demonstrated that the elastic behaviors of rebar could be well simulated by the mesoscopic axisymmetric RBSM. Red

curve in **Fig. 10(b)** showed the calculated Poisson's ratio by simulating the compression test of pure concrete with 2D plane stress RBSM by Nagai et al. [21]. In their study, it had been successfully proved that the Poisson's ratio of concrete (around 0.2) could be well simulated with the two-dimensional RBSM. In the current study, the simulation results indicated that the developed mesoscale axisymmetric RBSM could successfully simulate the Poisson's ratio for reinforcement as well, see the black curve in **Fig. 10(b)**.

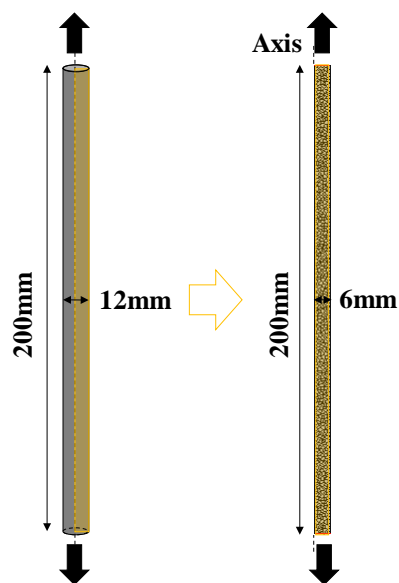


Fig. 9. Uniaxial tension test of rebar and axisymmetric RBSM model

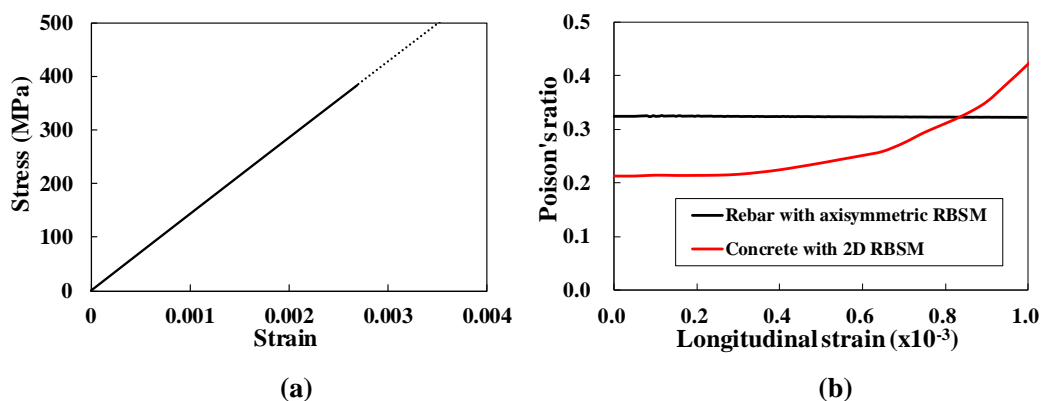


Fig. 10. Elastic behaviors of reinforcement by axisymmetric RBSM simulation

4.2.2 Bond behaviors of non-damaged specimens

After simulating the pulling-out test, the average bond stress τ was calculated by Eq. (28) where P , D and l_a was the applied load, rebar diameter and anchorage length [18]. The slip between reinforcement and concrete was defined as the displacement of the loading end (bottom surface of the reinforcement). The bond-slip behaviors of non-damaged specimens were drawn in **Fig. 11**. From **Fig. 11**, it was indicated that for same concrete strength (C35), the calculated bond strength showed slightly decreasing with larger embedment length. Meanwhile, for specimens with the same embedment length (5D), the bond strength would increase by increasing the concrete strength grade.

This phenomenon matched well with the observation by Liu et al. [18]. The bond strength for all the cases (including the frost-damaged case in section 4.2.3) were listed in **Table 3** and plotted together with the experimental results, as shown in **Fig. 12**. Though the simulated bond strength showed a bit larger than the test data, but they were still considered to be correlated since the experimental results showed larger scattering (up to 24.8%) according to Liu et al. [18].

$$\tau = \frac{P}{\pi dl_a} \quad (28)$$

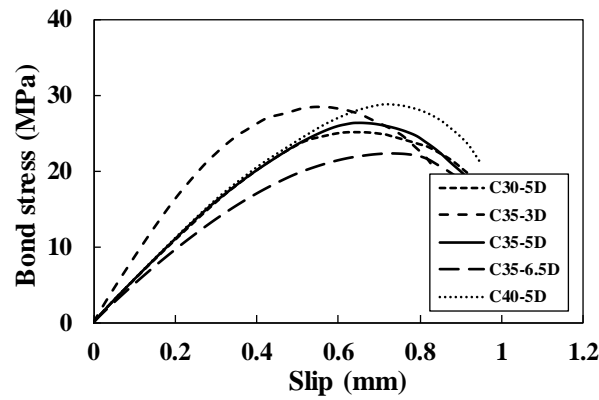


Fig. 11. Bond stress-slip curves of non-damaged specimens by axisymmetric RBSM

Table 3. Bond strength by Liu et al. 2016 and RBSM

Specimens	τ_u (MPa)		Cov. (%)
	Test	RBSM	
C30-5D	22.35	25.14	11.09
C35-3D	26.85	28.34	5.26
C35-5D	24.80	26.41	6.09
C35-6.5D	22.70	22.29	2.12
C40-5D	26.43	28.83	8.32
C35-5D-30	22.42	24.04	6.73
C35-5D-60	20.67	21.35	3.18
C35-5D-100	15.94	15.93	0.06

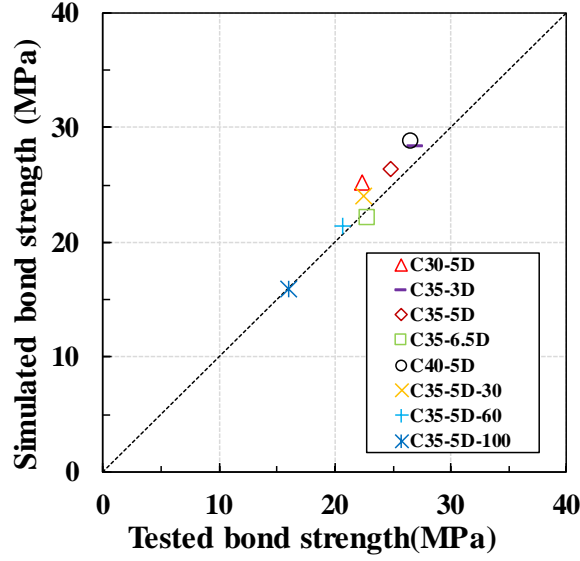


Fig. 12. Comparison of bond strength by experiment and axisymmetric RBSM

4.2.3 Bond behaviors of frost-damaged specimens

The deformations and meso-cracks of all specimens after different freezing-thawing cycles were drawn in Fig. 13 and 14, where the deformations in Fig. 13 were enlarged by 100 times and the short red lines in Fig. 14 meant the crack width of the corresponding normal spring had reached 0.005 mm. From Fig. 13 and 14, it could be observed that the frost action would lead to meso-cracks and expansive deformations in concrete [6-8]. Besides, meso-cracks initiated firstly along ITZ and bond regions since they played as the weakest parts. Especially for the specimen suffering 100 FTCs, obvious meso-cracks could be found between reinforcement and concrete (see Fig. 13(d) and Fig. 14(d)), which would diminish the bond strength. It should be also emphasized that since the spring length of bond interface was less than that of ITZ between mortar and aggregate, Fig. 14(d) also yielded that the tensile strain (damage) of bond interface was larger than that of ITZ between mortar and aggregate.

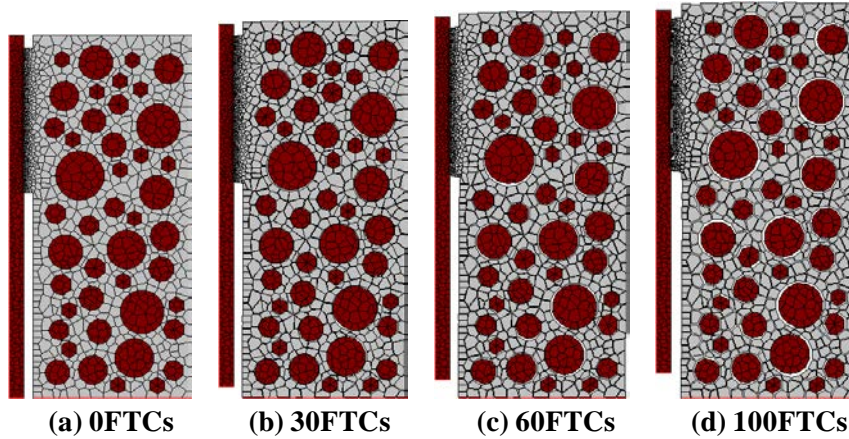


Fig. 13. Deformations of the specimens after FTCs (enlarged by 100 times)

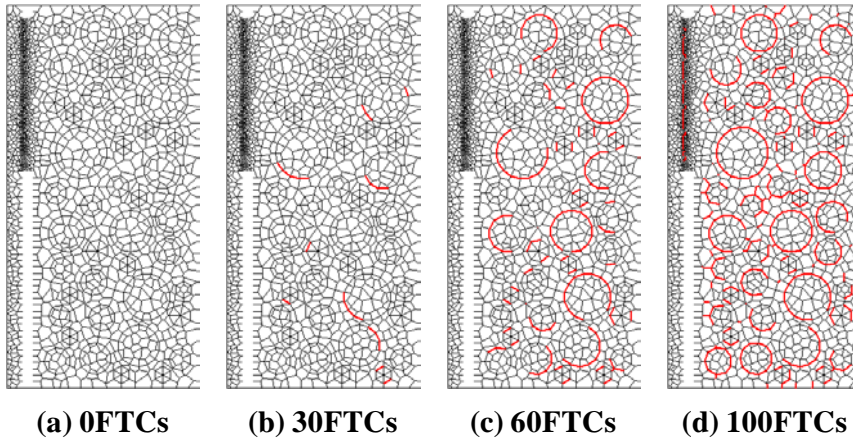


Fig. 14. Meso-cracks (=0.005 mm) of the specimens after FTCs

The simulated bond-slip behaviors of frost-damaged specimens were drawn in **Fig. 15** and the degradation of bond strength were plotted in **Fig. 16** together with the experimental results. It was indicated that the frost damage had obvious effects on the bond behaviors: both bond strength and stiffness showed reduction with increasing numbers of freezing-thawing cycles while the slip at peak bond stress increased slightly in the first few FTCs and decreased later. The slip at peak bond stress showed different behaviors with previous experimental results, which needed further examinations [1, 2, 15, 17, 18]. From **Fig. 16** where the analytical and experimental results were plotted and compared, correlation between the mesoscale axisymmetric RBSM simulation and experimentation could be found on the degradation of bond strength, which strongly demonstrated that the developed program in the current study could predict the degradation of bond strength under the effect of frost damage. The cracking patterns in z-r plane when normal springs reached the maximum bond stress were shown in **Fig. 17**, where the short red lines meant that the width of cracks had reached 0.005 mm in the corresponding normal springs. From **Fig. 17**, with more cycles of freezing-thawing, the diagonal cracks would penetrate deeper into concrete from bond interface and connect with the meso-cracks in concrete which were generated by the frost action.

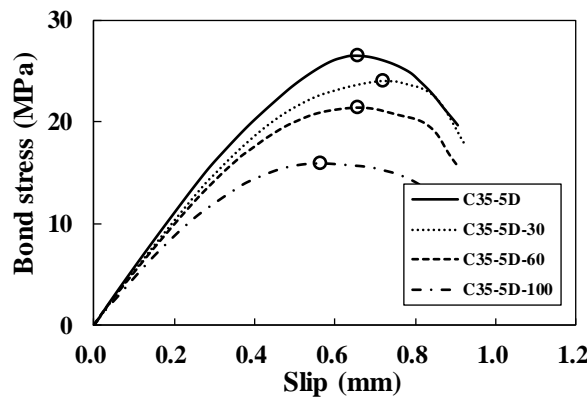


Fig. 15. Bond stress-slip curves for both sound and damaged specimens by RBSM

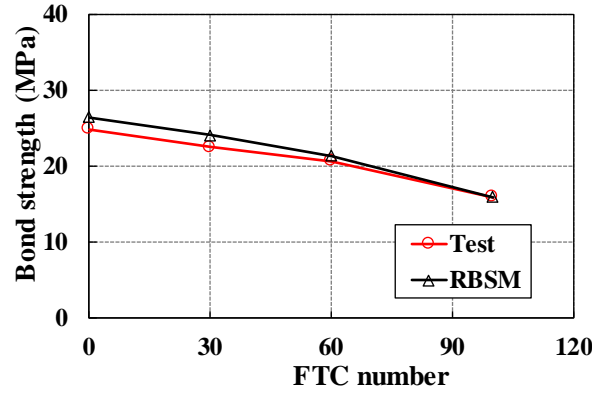


Fig. 16. Comparison of bond strength degradation between experiment and RBSM

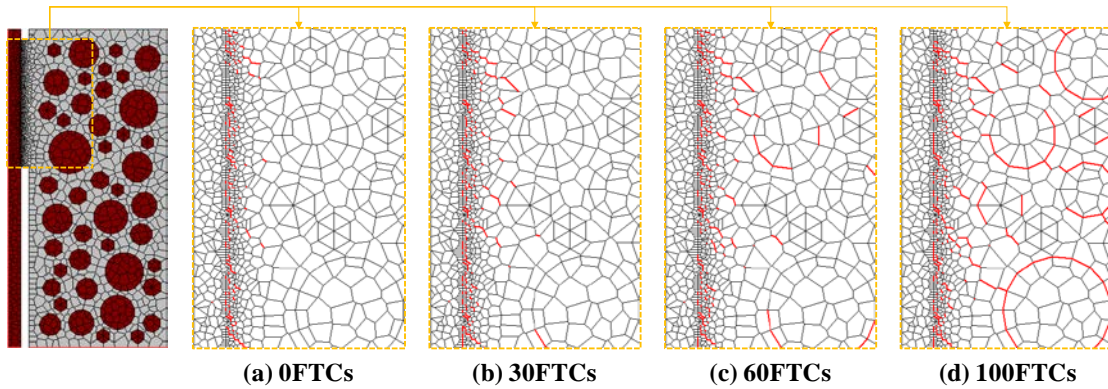


Fig. 17. Cracking patterns of the specimens at maximum bond stress

5. Conclusions

- (1) The mesoscale axisymmetric Rigid Body Spring Method program was successfully developed to analyze the macroscopic pulling-out behaviors of specimens with short embedment length under the effect of frost damage. Axisymmetric stiffness matrix was derived for RBSM and theoretical micro-meso mechanical models accounting for frost damage were applied into the program.
- (2) Reliability and applicability of the newly developed program were verified by conducting simulation of compressive test for pure concrete under FTCs. Prediction of compressive strength degradation was compared with previous 2D RBSM simulation as well as the available experimental data where satisfactory agreements were achieved. Besides, the elastic behaviors of reinforcement were also examined for the pulling-out simulation. As an important factor which affected the bond-slip behaviors, the Poisson's ratio of reinforcement was proved to be successfully simulated by the newly developed mesoscale axisymmetric RBSM.
- (3) Simulation of pulling-out test for short embedment specimens was conducted with the new program. For non-damaged specimens, the macroscale bond-slip behaviors could be well simulated with different cases (e.g. concrete strength and embedment length), which showed the reliability of the program. For frost-damaged specimens, the degradation of bond strength was observed in good correlation with experimental data, which proved that the developed mesoscale program could be adopted to predict the bond degradation

between reinforcement and concrete under the effect of frost damage.

Acknowledgements

The authors would like to acknowledge the Grand-in-Aid for Scientific Research (A) of Japan Society of Promotion of Science (No. 26249064) and scholarship from Ministry of Education, Culture, Sports Science and Technology-Japan (MEXT).

References

- [1] K.Z. Hanjari, P. Utgenannt, K. Lundgren, Experimental study of the material and bond properties of frost-damaged concrete, *Cement and Concrete Research*. 41 (3) (2011) 244-254.
- [2] S. Xu, A. Li, H. Wang, Bond properties for deformed steel bar in frost-damaged concrete under monotonic and reversed cyclic loading, *Construction and Building Materials*. 148 (2017) 344-358.
- [3] G.W. Scherer, J. Valenza, Mechanisms of frost damage, *Materials Science of Concrete*. 7 (60) (2005) 209-246.
- [4] O. Coussy, P.J. Monteiro, Poroelastic model for concrete exposed to freezing temperatures, *Cement and Concrete Research*. 38 (1) (2008) 40-48.
- [5] F. Gong, E. Sicat, D. Zhang, T. Ueda, Stress analysis for concrete materials under multiple freeze-thaw cycles, *Journal of Advanced Concrete Technology*. 13 (3) (2015a) 124-134.
- [6] M. Hasan, H. Okuyama, Y. Sato, T. Ueda, Stress-strain model of concrete damaged by freezing and thawing cycles, *Journal of Advanced Concrete Technology*. 2 (1) (2004) 89-99.
- [7] E. Sicat, F. Gong, D. Zhang, T. Ueda, Change of the coefficient of thermal expansion of mortar due to damage by freeze thaw cycles, *Journal of Advanced Concrete Technology*. 11 (12) (2013) 333-346.
- [8] F. Gong, Y. Wang, D. Zhang, T. Ueda, Mesoscale simulation of deformation for mortar and concrete under cyclic freezing and thawing stress, *Journal of Advanced Concrete Technology*. 13 (6) (2015b) 291-304.
- [9] Z. Wang, F. Gong, D. Zhang, H. Hayashida, T. Ueda, Mesoscale simulation of concrete behavior with non-uniform frost damage with verification by CT imaging, *Construction and Building Materials*. 157 (2017) 203-213.
- [10] A. Duan, W. Jin, J. Qian, Effect of freeze-thaw cycles on the stress-strain curves of unconfined and confined concrete, *Materials and Structures*. 44 (7) (2011) 1309-1324.
- [11] H.S. Shang, Y.P. Song, Experimental study of strength and deformation of plain concrete under biaxial compression after freezing and thawing cycles, *Cement and Concrete Research*. 36 (10) (2006) 1857-1864.
- [12] D. Cao, L. Fu, Z. Yang, X. Qin, Study on constitutive relations of compressed concrete subjected to action of freezing-thawing cycles, *Journal of Building Materials*. 16 (1) (2013) 17-23.
- [13] Z. Wang, D. Zhang, F. Gong, T. Ueda, Modeling of mechanical behavior of concrete with frost damaged based on 2D rigid body spring model, 8th Asia and Pacific Young Researchers and Graduates Symposium. Tokyo, 2017.
- [14] K.Z. Hanjari, P. Kettil, K. Lundgren, Modelling the structural behavior of frost-damaged reinforced concrete structures, *Structure and Infrastructure Engineering*. 9 (5) (2013) 416-431.
- [15] T.S. Shih, G.C. Lee, K.C. Chang, Effect of freezing cycles on bond strength of concrete, *Journal of Structural Engineering*. 114 (3) (1988) 717-726.
- [16] L. Peterson, L. Lohaus, M.A. Polak, Influence of freezing-and-thawing damage on behavior of

reinforced concrete elements, *ACI Materials Journal*. 104 (4) (2007) 369-378.

[17] X. Ji, Y. Song, Y. Liu, Effect of freeze-thaw cycles on bond strength between steel bars and concrete, *Journal of Wuhan University of Technology-Mater. Sci. Ed.* 23 (4) (2008) 584-588.

[18] Y. Liu, F. Chen, W. Wang, Z. Li, Bond performance of thermal insulation concrete under freeze-thaw cycles, *Construction and Building Materials*. 104 (2016) 116-125.

[19] M. J. Setzer, Capillary suction, internal damage and freeze-thaw test-reference method and alternative methods A and B (RILEM TC 176 IDC), *Material and Structures*. 34 (2001) 515-525.

[20] T. Kawai, New discrete models and their application to seismic response analysis of structures, *Nuclear Engineering and Design*. 48 (1) (1978) 207-229.

[21] K. Nagai, Y. Sato, T. Ueda, Mesoscopic simulation of failure of mortar and concrete by 2D RBSM, *Journal of Advanced Concrete Technology*. 2 (3) (2004) 359-374.

[22] F. Gong, T. Ueda, Y. Wang, D. Zhang, Z. Wang, Mesoscale simulation of fatigue behavior of concrete materials damaged by freeze-thaw cycles, *Construction and Building Materials*. 144 (2017) 702-716.

[23] International Federation for Structural Concrete, *Fib model code for concrete structures 2010*, Berlin: Ernst & Sohn. (2013).

[24] J.E. Bolander Jr, S. Saito, Fracture analyses using spring networks with random geometry, *Engineering Fracture Mechanics*. 61 (5-6) (1998) 569-591.

[25] S. Muto, H. Nakamura, T. Tanabe, W. Srisoros, S. Lee, Analysis of bond characteristics between concrete and deformed bar by meso-scale analysis, *Journal of Applied Mechanics*. 7 (2004) 767-774.

[26] K. Nagai, Y. Sato, T. Ueda, Mesoscopic simulation of failure of mortar and concrete by 3D RBSM, *Journal of Advanced Concrete Technology*. 3 (3) (2005) 385-402.

[27] T. Ueda, M. Hasan, K. Nagai, Y. Sato, L. Wang, Mesoscale simulation of influence of frost damage on mechanical properties of concrete, *Journal of Materials in Civil Engineering*. 21 (6) (2009) 244-252.

[28] D. Hayashi, K. Nagai, L. Eddy, Mesoscale analysis of RC anchorage performance in multidirectional reinforcement using a three-dimensional discrete model, *Journal of Structural Engineering*, 143 (7) (2017) 04017059.

[29] N. Takeuchi, M. Ueda, T. Kawai, An analysis of axisymmetric problems by means of new discrete models, *Kenkyu Sokuho*. 32 (6) (1980) 31-34.

[30] B. Yao, W. Murray, Study of concrete cracking and bond using a distributed discrete crack finite element model, *ACI Materials Journal*. 92 (1) (1995) 93-104.

[31] A. Kambayashi, H. Kobayashi, K. Sonoda, Applicability of a rigid body spring model to impact problems of axi-symmetric elastic bodies, *Journal of Applied Mechanics*. 2 (1999) 271-278.

[32] F. Gong, T. Ueda, D. Zhang, Two-dimensional rigid body spring method based micro-mesoscale study of mechanical strengthening/damaging effects to concrete by frost damage, *Structural Concrete*. 19 (4) (2018) 1131-1145.

[33] Y. Xi, Z.P. Bazant, H.M. Jennings, Moisture diffusion in cementitious materials Adsorption isotherms, *Advanced Cement Based Materials*. 1 (6) (1994) 248-257.

[34] Z. Sun, G. W. Scherer, Effect of air voids on salt scaling and internal freezing temperatures, *Cement and Concrete Research*. 40 (2) (2010) 260-270.

[35] E. Sicat, F. Gong, T. Ueda, D. Zhang, Experimental investigation of the deformational behavior of the interfacial transition zone (ITZ) in concrete during freezing and thawing cycles, *Construction*

- 1 and Building Materials. 65 (2014) 122-131.
- 2 [36] Japan Society of Civil Engineers, Standard specification for concrete structures, Tokyo: JSCE.
- 3 (2007).